Measuring dielectric properties at the nanoscale using Electrostatic Force Microscopy

R. Arinero[1], C. Riedel[1,2,3], G. A. Schwartz[4], G. Lévêque[1], A. Alegría[3,4], Ph. Tordjeman[5], N. E. Israeloff[6], M. Ramonda[7] and J. Colmenero[2,3,4]

[1] IES, UMR CNRS 5214, Université Montpellier II, CC 083, Place E. Bataillon, 34095 Montpellier Cedex, France
[2] Donostia International Physics Center (DIPC), Paseo Manuel de Lardizábal 4, 20018 San Sebastián, Spain.
[3] Departamento de Física de Materiales UPV/EHU, Facultad de Química, Apartado 1072, 20080 San Sebastián, Spain.
[4] Centro de Física de Materiales CSIC-UPV/EHU, Paseo M. De Lardizábal 5, 20018 San Sebastián, Spain.
[5] IMFT, Université de Toulouse – CNRS, 1 Allée du Professeur Camille Soula, 31400 Toulouse, France.
[6]Department of Physics, Northeastern University, Boston, Massachusetts 02115, USA
[7]Laboratoire de Microscopie en Champ Proche (LMCP), Centre de Technologie de Montpellier, Université Montpellier II, CC 082, Place E. Bataillon, 34095 Montpellier Cedex, France

Several electrostatic force microscopy (EFM) – based methods have been recently developed to study the nanoscale dielectric properties of thin insulating layers. Some methods allow measuring quantitatively the static dielectric permittivity whereas some others provide qualitative information about the temperature-frequency dependence of dielectric properties. In this chapter, all these methods are described and illustrated by experiments on pure and nanostructured polymer films. A section is dedicated to EFM probe – sample models and especially to the Equivalent Charge Method (ECM).

Keywords Atomic Force Microscopy; Electrostatic Force Microscopy; dielectric; local properties; nanoscale; polymer; dynamics; glass transition; imaging .

1. Introduction

Broadband Dielectric Spectroscopy (BDS) has shown to be a very useful, extended and versatile technique to study dielectric materials and in particular polymers and other glass formers. Recent advances have made it possible to probe the dynamics of thin polymer films (with a thickness as low as 5nm), opening the area of interfaces studies [1], [2]. However, BDS has a fundamental limitation: it has no spatial resolution. This is usually not a problem when homogeneous and non-structured systems are analyzed but it becomes an important limitation for studying the local properties of heterogeneous and/or nano-structured materials. To overcome this constrain different methods have been recently developed to measure the nanoscale dielectric properties of thin films by means of Electrostatic Force Microscopy (EFM). Some methods allow studying quantitatively the static dielectric properties whereas some others permit to obtain qualitative information on the temperature-frequency dependent dielectric properties. All these methods were first adapted for measurements in one point. The passage from single point to the mapping of a heterogeneous material has been possible thanks to both numerical and experimental advances. Some previous related works have been published during the last years. We can mention for instance the works of Krayev *et al* [3], [4] related to the study of polymers blend in the form of layer of several microns thickness. These authors showed that an electric contrast could be obtained on EFM images and that such a contrast is related to the variations of the relative dielectric permittivity ε_r. They also quantified the value of ε_r in the frame of a simple spherical capacitor model. Unfortunately, this model is appropriate only under certain conditions because it makes the approximation that the thickness of the sample is very large compared with the tip radius and the tip-sample distance. Moreover, dielectric constants of two reference polymers are required to measure a third unknown one. On the other hand, Fumagalli *et al* have developed the so-called "Nanoscale Capacitance Microscopy" [5], where the microscope is equipped with a sub-attofarad low-frequency capacitance detector. The same group also proposed a method based on the detection of the DC electrostatic force to image the dielectric constant of a purple membrane patch [6]. In this chapter, we present the specificities of some EFM based methods, which can be operated either by detecting the force or the force gradient between the probe and the sample, and by applying either DC or AC voltages. A section is dedicated to probe-sample electrostatic interaction modeling using the Equivalent Charge Method (ECM). Compared to existing analytical models, this numerical method allows calculating the probe-sample capacitance without any geometrical restrictions on the probe shape and dielectric film thickness. We also present recent results, illustrating the multiple potential applications of these different methods. Among these applications we focus on the quantitative determination of the nanoscale static dielectric permittivity of polymer films at different temperature [7] and the quantitative mapping of the dielectric constant of a phase separated polymer blend [8]. Finally, we show how it is possible to extend the measurement of the frequency dependence of the dielectric response in one single point [9], [10] to image the dynamics of a heterogeneous polymer blend [11].

2. Modeling of the probe-sample interaction in electrostatic force microscopy

2.1 Brief historical review of existing models

A number of models describing probe-sample interactions have been proposed in the two last decades. Earlier models treated the probe surface as an equipotential with an assumed distribution of charges, such as a single point charge [12] or a uniformly charged line [13], and the probe-sample interaction was approximated as the interaction between the assumed charge distribution and its image with respect to the sample surface. Another group of models introduced geometric approximations to the probe shape and solved the probe-sample capacitance problem either by exactly solving the boundary value problem, e.g., the sphere model [14] and the hyperboloid model [15], or by introducing further approximations to the electric field between the probe and the sample [16-18]. These models provide convenient analytic expressions of the probe-sample interaction; however, more sophisticated models are demanded for studying the lateral variation of the sample surface properties (e.g., topography and trapped charges distribution) or to take into account the presence of a dielectric film of variable thickness. Let us consider the AFM tip as a cone of half angle θ_0, with a spherical apex of radius R, attached to the extremity of a cantilever, the total capacitance $C(z)$ versus the tip-sample distance z is the sum of the apex capacitance $C_{apex}(z)$, i.e the local capacitance, and the stray capacitance $C_{stray}(z)$, associated with the tip cone and the cantilever contributions. For films thicknesses less than 100 nm we can refer to the model proposed by Fumagalli *et al* [19]. It can be expressed as:

$$C_{apex}(z) = 2\pi\varepsilon_0 R \ln\left(1 + \frac{R(1-\sin\theta_0)}{z + h/\varepsilon_r}\right) \tag{1}$$

where h and ε_r are the thickness and the relative dielectric constant of the layer, respectively. By fitting the region where the effect of the local capacitance is negligible, they found a stray capacitance of the linear form $C_{stray}(z) = -b.\Delta z$. A second family of models, also called Equivalent Charge Method (ECM), replaced the probe and the sample by a series of point charges and/or line charges and their image charges [20-23]. Based on this method, interactions between the probe and a conductive or dielectric sample with topographic and/or dielectric inhomogeneities [24-26] have been studied. This approach was capable of accommodating different scenarios. The third family of approaches used numerical methods such as the finite element method [27], the self-consistent integral equation method [28], and the boundary element method [29]. The main advantage of these models is their ability to take into account the exact geometry of the EFM probe, which permits comparison of different probe tip shapes.

2.2 The Equivalent Charge Method (ECM)

In this section, we show how the probe-sample force, force gradient and capacitance can be calculated using the Equivalent Charge Method (ECM). The advantage of numerical simulation compared to other analytical expression is that the calculated force is exact and allows to work without any restriction about the thickness of the insulating film, the tip radius and the tip-sample distance. We will first consider the case of a tip in front of a metallic plate, and then we will deduce the force and the force gradient for a system composed by a tip in front of a dielectric layer over a metallic plate.

The case of a system composed by a tip in front of a conductive plane has been treated by Belaïdi *et al.* [21]. The idea of ECM is to find a discrete charge distribution (N_C charge points q_i at a distance z_i on the axis x=0) that will create a given potential V at the tip surface. The tip geometry is represented by a half of sphere of radius R surmounted on a cone with a characteristic semi-angle $\theta_0 = 15°$. The conductive plane at a zero potential is created by the introduction of an electrostatic image tip with $-q_i$ charges at a distance $-z_i$ on the z axis (Fig. 1a).

The value of the charges q_i is fixed in such way that the M potential V_n, with $n = 1,\ldots,M$, calculated at test point n at the tip surface are equal to V. If we introduce $D_{i,n} = \frac{1}{d_{i,n}} - \frac{1}{d^*_{i,n}}$ (where $d_{i,n}$ and $d^*_{i,n}$ are the distances between the point n and the effective and image charge i, respectively) we can express the potential V_n as:

$$V_n = \sum_i^{N_c} \frac{D_{i,n} q_i}{4\pi\varepsilon_0} \tag{2}$$

The best value of q_i is obtained using the least mean square method:

$$\frac{\partial}{\partial q_i}\sum_n^M (V_n - V)^2 = 0 \tag{3}$$

Expliciting the derivative of the potential, the system to solve becomes:

$$\sum_n^M \left(\sum_i^{N_c} \frac{D_{i,n} q_i}{4\pi\varepsilon_0} - V \right) \frac{D_{i,n}}{4\pi\varepsilon_0} = 0 \tag{4}$$

Then, knowing the charge and image charge distributions, the total electrostatic force acting on the tip and the tip-sample capacitance can be calculated.

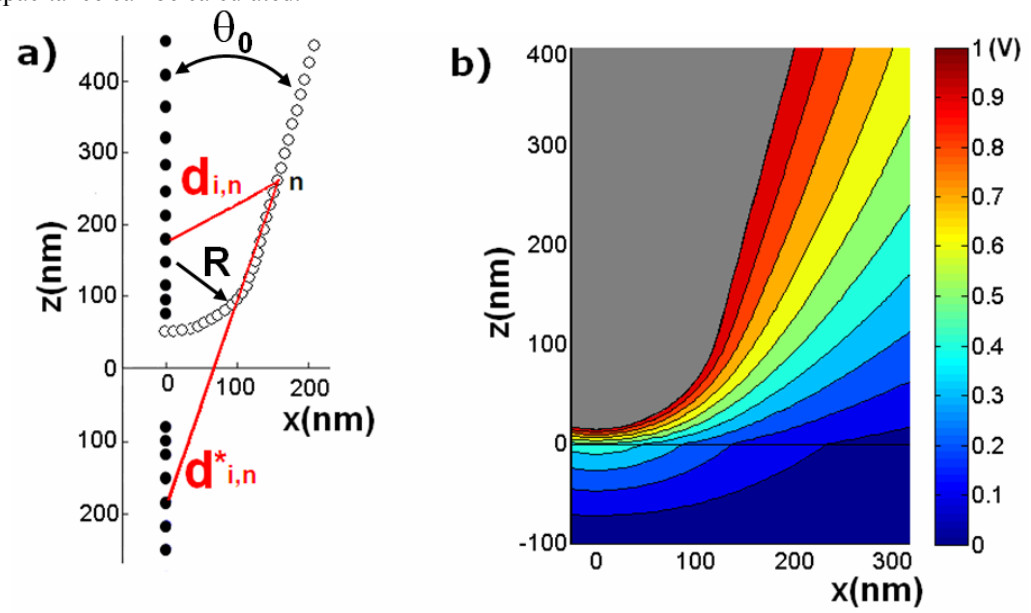

Fig. 1: a) Representation of the charges (● $z > 0$), image charges (● $z < 0$), and test points (○) modeling the tip over a metallic plate; b) potential, created in the air ($z > 0$) and in the dielectric ($z < 0$) by a tip (R = 130 nm, θ = 15°) in front of a dielectric layer of height h = 100 nm with a dielectric constant ε_r = 4. The potential is set to 1V at the surface of the tip. The maximum error in one test point is of the order of 1/1000. *Reproduced with permission from C. Riedel et al.[7] © Copyright 2009 American Institute of Physics.*

When the system is composed by a tip in front of a dielectric layer on a conductive substrate, simulations are more complex. This problem has been treated by Sacha *et al.* [22] introducing the Green function formalism and also by Durand [23]. We consider one charge q_i in the air at a distance z_i of a dielectric layer of thickness h and of dielectric constant ε_r. The insulating layer is placed over a conductive substrate. V_0^i and V_1^i are respectively the potentials created by the charge q_i in the air and in the dielectric. In order to satisfy the limit conditions ($V_0^i = V_1^i$ and $\varepsilon_0 \frac{\partial V_0^i}{\partial z} = \varepsilon_O \varepsilon_r \frac{\partial V_1^i}{\partial z}$ at the air/dielectric interface, and, $V_1^i = 0$ at the dielectric/substrate interface), we introduce two series of image charges, one created in the conductive substrate and one in the air.

The equivalent potential calculated by ECM in the air results from the source, its image in the dielectric and the infinite series of image charges in the conductive substrate. One can introduce the "reciprocal distance", $D+$, between a point of coordinate (ρ,z) and the charge q_i (id. its image ($D-$), $D\pm = \frac{1}{\sqrt{\rho^2 + (z \mp z_i)^2}}$), and the reciprocal distance A corresponding to the infinite series of image ($A = \sum_{n=0}^{\infty} \frac{k^n}{\sqrt{\rho^2 + (z + 2(n+1)h + z_i)^2}}$, where the constant $k = -\frac{\varepsilon_r - 1}{\varepsilon_r + 1}$). Then, the potential V_0^i created in the air by one charge q_i is expressed as:

$$V_0^i = \frac{q_i}{4\pi\varepsilon_0}\left(D_+ + kD_- - (1-k^2)A\right) \quad (5)$$

The potential V_1^i created in the dielectric is the sum of the two infinite series of images. Introducing the reciprocal distance for the images in the conductive substrate, B ($B = \sum_{n=0}^{\infty} \frac{k^n}{\sqrt{\rho^2 + (z - 2nh - z_i)^2}}$), we obtain:

$$V_1^i = \frac{q_i}{4\pi\varepsilon_0}(1-k)(B-A) \quad (6)$$

The value of each q_i is then found by solving Eq. 3, inserting the potential V_0^i calculated after Eq. 5, at each test point representing the tip surface. Knowing the charge and image charge distributions, the total electrostatic force acting on the tip and the tip-sample capacitance can be calculated. In Fig. 1 b), we present the repartition of the equipotentials in air and in a dielectric layer ($\varepsilon_r = 4$) for h = 100 nm.

3. Electrostatic force microscopy (EFM) experiments

3.1 EFM basic principles

Electrostatic force microscopy (EFM) is one of the Scanning Probe Microscopy families, first implemented by Martin et al [30] in 1988, which is generally used to image localized charges on surfaces [31] and to measure the surface potential on semiconducting materials [32].

Let us consider the case of a thin dielectric film sample deposited on a conductive substrate. When a voltage V_{app} is applied to the probe (with the sample holder grounded), the electrostatic force F_{el} involved in EFM signals can be written as:

$$F_{el} = \frac{1}{2}\frac{\partial C}{\partial z}\left(V_{app} + V_{CP}\right)^2 \quad (7)$$

V_{CP} is the contact potential difference between the probe and the substrate, corresponding to the work function difference of both materials. C is the probe-sample-substrate capacitance. As shown in the previous section, it is a function $C(R, \theta_0, \varepsilon_r, h, z)$ of many parameters: the probe geometry, described by the tip radius R and the cone semi-angle θ_0, the sample dielectric permittivity ε_r, the sample thickness h and the probe-surface distance z.

DC and AC voltages can be applied simultaneously or separately, in such way that $V_{app} = V_{DC} + V_{AC}\sin\omega_e t$, where ω_e is the angular frequency of the electrical excitation. Then, F_{el} exhibits a DC component and two oscillating AC components at ω_e and $2\omega_e$:

$$\begin{cases} F_{DC} = \frac{1}{2}\frac{\partial C}{\partial z}\left[\left(V_{DC} + V_{CP}\right)^2 + \frac{V_{AC}^2}{2}\right] \\ F_{\omega_e} = \frac{\partial C}{\partial z}\left(V_{DC} + V_{CP}\right)V_{AC}\sin\omega_e t \\ F_{2\omega_e} = \frac{1}{4}\frac{\partial C}{\partial z}V_{AC}^2\cos 2\omega_e t \end{cases} \quad (8)$$

The DC component is a static attractive force between the electrodes composing the capacitor, the ω_e component has a single linear dependence on the capacitive coupling $\partial C/\partial z$ and the contact potential difference V_{CP}, and the $2\omega_e$ component is a force induced to the capacitor only by the AC voltage. The ω_e component disappears when appropriate bias voltage is applied to the probe to cancel V_{CP}, i.e., $V_{DC}+V_{CP}=0$. V_{CP} can be therefore quantitatively measured by the feedback control of V_{DC} to maintain the ω_e component to be zero. This protocol is known as Kelvin probe force microscopy (KPFM) [32]

A similar reasoning can be made when detecting the electrostatic force gradient G_{el}, equal to the first derivative of the force:

$$G_{el}=\frac{1}{2}\frac{\partial^2 C}{\partial z^2}\left(V_{app}+V_{CP}\right)^2 \tag{9}$$

G_{el} exhibits a DC component and two oscillating AC components at ω_e and $2\omega_e$:

$$\begin{cases} G_{DC}=\dfrac{1}{2}\dfrac{\partial^2 C}{\partial z^2}\left[\left(V_{DC}+V_{CP}\right)^2+\dfrac{V_{AC}^2}{2}\right] \\ G_{\omega_e}=\dfrac{\partial^2 C}{\partial z^2}\left(V_{DC}+V_{CP}\right)V_{AC}\sin\omega_e t \\ G_{2\omega_e}=\dfrac{1}{4}\dfrac{\partial^2 C}{\partial z^2}V_{AC}^2\cos 2\omega_e t \end{cases} \tag{10}$$

The main advantage in detecting electrostatic gradients instead of forces is to enhance by about 30% the spatial resolution, as demonstrated in ref [33].

EFM operations are the most of time realized using dynamics AFM modes, i.e. modes where the cantilever vibrates near or at its resonance frequency. Among them, amplitude-modulation-AFM (AM-AFM), well known as Tapping® mode, is widely used in commercial instruments, under room conditions. While maintaining constant the excitation pulsation ω_m, the amplitude of vibration of the cantilever decreases when approaching the surface due to attractive interactions. The amplitude of vibration serves as feedback parameter for topography acquisition. EFM operations with AM-AFM can be associated with double-pass scans (lift-mode®) where the topographic information is obtained during the first pass and the electrostatic signals are acquired during the second pass [7], [8]. This method has the key advantage to avoid any coupling effects between structural and dielectric information, and to allow setting optimized conditions for electric measurements (linear regime). The second dynamic mode, frequency-modulation-AFM (FM-AFM), also called non-contact AFM, is generally used under vacuum where Q-factors of cantilevers are too high to obtain a short transient regime of the vibration. In that case, the probe-sample distance is controlled by fixing a small negative shift of the resonance frequency caused by attractive interactions with the surface. This frequency shift serves as feedback parameter for the formation of topographic images. For instance, FM-AFM is not associated with double-pass scans. The electrostatic signal is acquired simultaneously with topography [9]-[11]. EFM operations are in rare cases made using static AFM modes [6].

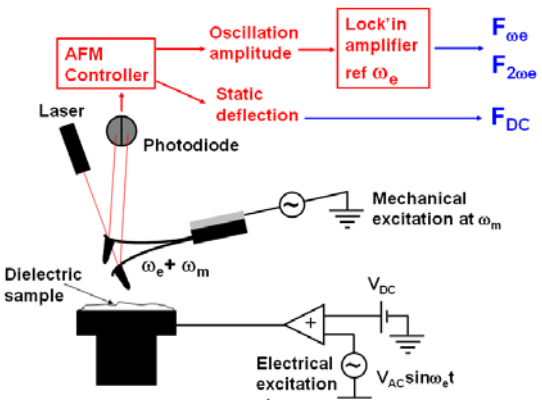

Fig 2: Experimental set-up for electrostatic forces detection

We will detail in the following sections all the different possibilities for doing EFM measurements of dielectrics. For a better classification, we will first separate EFM operations in 2 categories: Force and Force gradient detection methods.

Force detection methods are relatively simple to be implemented. A typical set-up is presented in Fig. 2. The DC component F_{DC} can be directly obtained from the static deflection signal. F_{ω_e} and $F_{2\omega_e}$ components can be extracted analysing the

oscillation amplitude by a lock-in amplifier, with the electrical excitation as reference signal.

Concerning to the force gradient detection methods, if we consider that the cantilever-tip-sample system can be approximated by a spring mass system having a resonance frequency f_0, the relationships between frequency shifts Δf_0 or mechanical phase shifts $\Delta\Phi_m$ and electrostatic force gradient G_{el} (assuming $G_{el} << k_c$ and $\tan\Delta\Phi_m \cong \Delta\Phi_m$) can be written as [34]:

$$\frac{\Delta f_0}{f_0} \cong -\frac{1}{2}\frac{G_{el}}{k_c} \quad , \tag{11}$$

$$\Delta\Phi_m \cong -\frac{Q}{k_c}G_{el} \quad , \tag{12}$$

where k_c and Q are the stiffness of the cantilever and the quality factor, respectively.

There are two possibilities to detect the local electrostatic force gradient. The first one is to measure directly the resonance frequency shift Δf_0 keeping the phase shift constant. The second possibility is to measure the mechanical phase shift $\Delta\Phi_m$ at constant driving frequency. We often prefer to measure frequency shifts because, relation (12) is valid only at low voltages (and becomes non linear at high voltages), whereas relation (11) is always valid. A typical set-up is shown in Fig. 3. Δf_0 and $\Delta\Phi_m$ signals are provided by most of commercial AFM controller electronics and can be directly linked to G_{DC}. To obtain G_{ω_e} and $G_{2\omega_e}$ components, Δf_0 or $\Delta\Phi_m$ signals have to be demodulated by means of a lock-in amplifier.

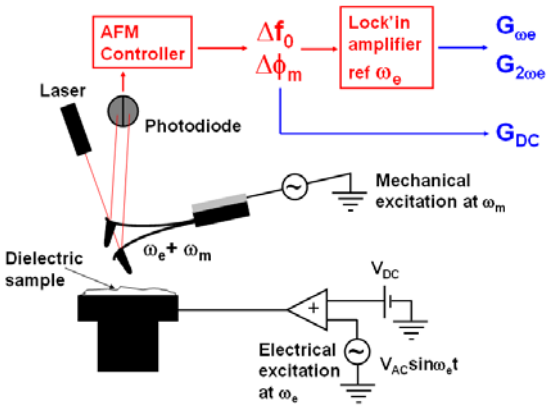

Fig 3: Experimental set-up for electrostatic force gradients detection

3.2 DC experiments

Let us now consider experiments where only DC voltages are applied. As expected from relations (11) the curves $\Delta f_0(V_{DC})$ have the parabolic shape $-a_{\Delta f_0}(z)V_{DC}^2$, where $a_{\Delta f_0}(z)$ is related to the tip-sample capacitance by the expression:

$$a_{\Delta f_0}(z) = \frac{f_0}{4k_c}\frac{\partial^2 C(z)}{\partial z^2} \tag{13}$$

The experimental protocol was performed on one single surface position on the basis of a "double pass method" and the measurement of $a_{\Delta f_0}(z)$ parabolic coefficient from the experimental curves $\Delta f_0(V_{DC})$.

During the first scan the topography is acquired in the AM-AFM mode. The tip is then retracted from the surface morphology by a constant height H_{lift}, also called "lift height", and the amplitude of the tip vibration δz is reduced in order to stay in the linear regime (amplitude << tip-sample distance). During the second scan, while a potential V_{DC} is applied to the tip (with the sample holder grounded) the electric force gradient G_{DC} is detected. As shown in Fig. 4 during the first scan, the average tip-sample distance z_1 is approximately equal to the oscillation amplitude ($z_1 \cong \delta z_1$). During the second scan, the distance is the sum of the first scan amplitude δz_1 and the lift height H_{lift} ($z_2 \cong \delta z_1 + H_{lift}$) while the cantilever oscillates with an amplitude of δz_2.

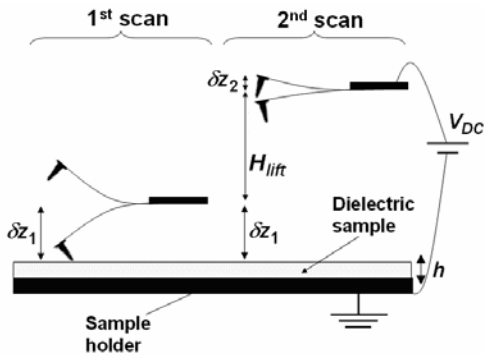

Fig. 4: Principle of the double pass method. During the first scan topography is acquired. The tip is then retracted by a constant height H_{lift} and amplitude is reduced by a factor of about 3. During the second scan, a potential V_{DC} is applied to the tip and G_{DC} is detected. *Reproduced with permission from C. Riedel et al.[7] © Copyright 2009 American Institute of Physics.*

The EFM experiments are performed in three steps: first, in order to determine the actual value of the tip radius R, we measure $\Delta f_0(V_{DC})$ curves at several lift height H_{lift} over a conductive sample. The parabolic fit gives the experimental coefficients $a_{\Delta f_0}(z)$ according to the real tip-sample distance. The value of the tip radius R is then obtained by fitting the $a_{\Delta f_0}(z)$ curve with expression (13) in which the tip-sample capacitance is calculated using the Equivalent Charge Model (ECM) (see the previous section). Second, the experiment is performed with a thin insulating layer of the material under study deposited on the conductive substrate. $\Delta f_0(V_{DC})$ curves are recorded at different lift heights H_{lift} and are analysed in order to extract experimental coefficients $a_{\Delta f_0}(z)$ for each lift height. Once R and h (the thickness of the sample measured by AFM) are known from previous experiments, we can fit the $a_{\Delta f_0}(z)$ curve using expression (13) in which the capacitance is calculated by ECM, and thereby we obtain the value of the dielectric permittivity ε_r.

Finally, in a third step, we record an amplitude-distance curve to quantify the actual values of δz_1 and z_2 in the previous force gradient experiments. It is worth to mention that the measurement of an amplitude-distance curve can damage the tip and should be done at the end. The slope of this curve gives the correspondence between the photodetector rms voltage and the real oscillation amplitude. Indeed, if there is no indentation of the tip into the sample, we can consider that amplitude is coarsely equivalent to the distance. The zero distance corresponds to the point where amplitude becomes null. The tip-sample distance is calculated as the difference between the z-position of the actuator corresponding to the amplitude set point and the z-position corresponding to the zero distance.
Nota bene: During the record of the amplitude-distance curve, the tip can be destroyed. It is thus recommend doing it at the end of the experiments. Consequently, the adjustable parameter is the lift height. It can vary from positive to negative values, the minimum value corresponding to the height where the tip is in the contact with the sample. In order to maintain the oscillation of the cantilever in a linear regime, it is convenient to choose a second scan amplitude of approximately 3 or 4 times smaller than δz_1, so $\delta z_2 \approx 6$nm.

3.2.1 Measurement of the nanoscale dielectric permittivity of polymer films at different temperatures

We turn now to EFM experiments performed on two ultra-thin polymer films at different temperatures [7]. PS (weight average molecular weight M_w = 70950 g/mol) and PVAc (M_w = 83000 g/mol) were chosen because both the dielectric strength and its temperature dependence are very different for these two polymers. Additionally, the dielectric responses of both polymers have been previously well characterized in the literature [35]-[39]. Samples were prepared by spin coating starting from solutions at 1% (w/w) in toluene. The substrate was composed of a fine gold layer deposited on a glass plate. The percentage of polymer in solution was selected in order to obtain films with a thickness of about 50 nm according to ref [40]. In this case standard EFM cantilevers were used having a free oscillating frequency f_0 = 71.42 kHz and a stiffness k_c = 4.4 N.m^{-1}. The experiments were performed on neat PS and PVAc films at room temperature and at 70°C (Fig. 5a and 5b). The measured thicknesses of the films were 50 ± 2 nm for PS and 50 ± 3 nm for PVAc at both room temperature and 70°C. The thicknesses were determined by AFM, measuring the height difference between the polymer surface and the gold substrate after the films were cut using a sharp steel knife. The accuracy of these measurements does not allow detecting any thermal expansion. The experimental parabolic coefficients $a_{\Delta f_0}(z)$ obtained for PS are shown in Fig. 5a. Measurements at room temperature and at 70°C are very close indicating a weak temperature dependence of the dielectric permittivity as expected for this polymer. In addition, there is a big difference between the curve obtained on gold and those obtained on PS. That means that the permittivity of the polymer is rather low. Using the same protocol, it is possible to obtain the value of the tip radius (R = 32±2 nm) and the dielectric permittivity of PS at 22°C and 70°C: $\varepsilon_r(22°C) = 2.2 \pm 0.2$ and $\varepsilon_r(70°C) = 2.6 \pm 0.3$. The experimental parabolic coefficients obtained for PVAc are shown in Fig. 5b. We can note a significant difference between measurements realized at room temperature and at 70°C, i.e. below and above the glass transition temperature, *Tg*. At 70°C, the PVAc curve approaches the gold curve indicating an important increase of ε_r. By applying ECM, values of

$\varepsilon_r(22°C) = 2.9 \pm 0.3$ and $\varepsilon_r(70°C) = 8.2 \pm 1.0$ were obtained for PVAc. The estimated values for PS and PVAc are in good agreement with the macroscopic ones [35]-[39]. The variation observed in the dielectric permittivity of PVAc is related with its strong dipole moment and the fact that PVAc crossed the glass transition temperature at around 38°C increasing the chain mobility and therefore the dielectric permittivity. Opposite, PS has a weak dipole moment and its *Tg* is around 105°C; therefore, a little or negligible variation of the dielectric permittivity is expected in this case.

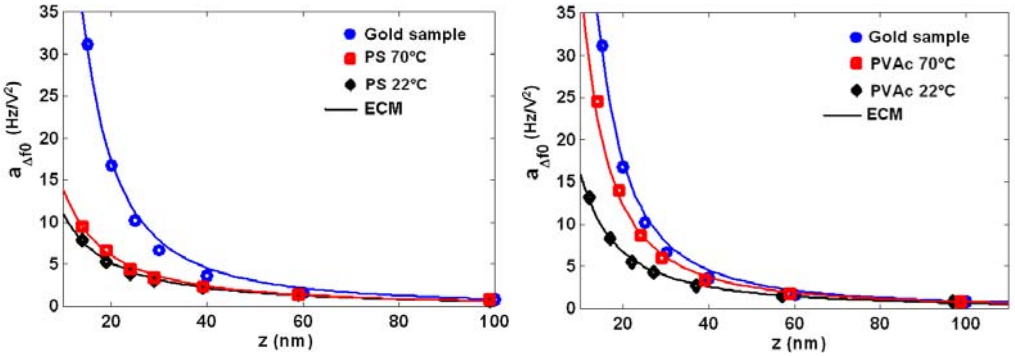

Fig. 5: a) $a_{\Delta f0}(z)$ curves obtained on a 50±3 nm PS thin film at 22°C (diamond) and 70°C (squares) in comparison with the curve obtained on a gold sample (circles). The tip radius R = 32±2 nm is obtained from experiments on gold using ECM. By fitting PS parabolic coefficients using ECM, values of ε_r = 2.2 ± 0.2 at 22°C, and ε_r = 2.6 ± 0.3 at 70°C are obtained. b) $a_{\Delta f0}(z)$ curves measured on a 50±2 nm PVAc thin film at 22°C (diamond) and 70°C (squares) in comparison with the curve obtained on a gold sample (circles). By fitting PVAc parabolic coefficients using ECM, values of ε_r = 2.9 ± 0.3 at 22°C and ε_r = 8.2 ± 1.0 at 70°C are obtained. *Reproduced with permission from C. Riedel et al.[7] © Copyright 2009 American Institute of Physics.*

3.2.2 Constant dieletric mapping of a nanostructured PVAc/PS polymer blend

Morphology and dielectric properties have been studied [8] on a model nanostructured soft material constituted by an immiscible blend of polystyrene (PS) and of poly(vinyl acetate) (PVAc) (PS: M_n=66900 g/mol and M_w=71000 g/mol ; PVAc: M_n=33200 g/mol and M_w=93100 g/mol). The sample film was prepared from a solution of the two polymers (1% w/w in toluene with 75% PS w/w and 25% w/w PVAc). The volume fraction of PVAc is $\Phi = 16.4\%$. The solution was subsequently spin-coated [40] on a conductive gold substrate at 3000 rpm. The film exhibits a nodular morphology of PVAc in a continuum phase of PS (Fig. 6a). The nodules of PVAc have a mean height measured by AFM around 50 nm and the PS a homogeneous thickness around 27 nm. Standard Pt-Ir coated tip were used for these measurements. The cantilever free resonance frequency was f_0=70.13 kHz and the stiffness k_c=4.5 N.m^{-1}. The tip radius was R=19±2 nm. Frequency shifts were measured by means of the succession of two double pass scans at a fixed value of the tip-sample distance, z_0=18±2 nm, and applying two different voltages of +5V and -5V. When the surface is characterized by a zero potential, only a single double pass scan is necessary to implement this method. However, it is recommended doing two double pass scans in order to verify the good accuracy of the measurements and to check the symmetry of the parabola with respect to the 0 V axis.

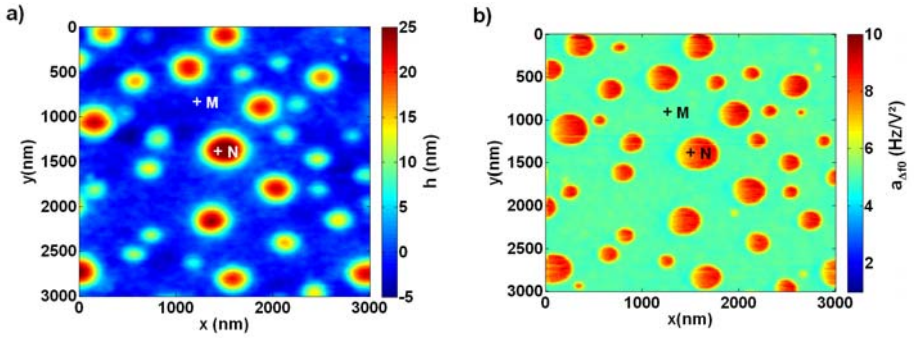

Fig 6: (a) Topography of the PVAc/PS film. (b) Corresponding map of the coefficient $a_{\Delta f_0}$. Values of h and $a_{\Delta f_0}$ at points M(PS) matrix and N(PVAc) nodule have been interpolated with ECM simulated curves in order to extract the corresponding value of ε_r. *Reproduced with permission from C. Riedel et al.[8] © Copyright 2010 American Physical Society.*

In the present study, the frequency shift at zero voltage was found to be nearly null in the scanned area. In order to ensure that the two frequency shifts correspond to the same sample point, the topography of the two images at different biases should be as similar as possible. However, working at 70 °C a non-negligible drift is observed. Translation effects have been numerically corrected by the introduction of a correlation function. Using these two measurements and assuming a zero frequency shift for zero voltage, the coefficient $a_{\Delta f_0}$ can be calculated at each point of the image. Fig. 6b presents the corresponding map of the coefficient $a_{\Delta f_0}$. In the general case, in order to take into account the nonzero contact potential V_{CP}, a third image has to be recorded at another applied voltage for example, at 0 V. A map of the parabolic coefficient $a_{\Delta f_0}$ could be obtained from the frequency shift images using the equation $\Delta f = a_{\Delta f_0}\left(V_{DC} - V_{CP}\right)^2$. From EFM results and ECM numerical simulations $a_{\Delta f_0}\left(h, \varepsilon_r\right)$ curves were calculated *at* each point of the image whereas the sample thickness h was determined by AFM (measuring the height difference between the polymer surface and the gold substrate). As an example, points M(PS) and N(PVAc) in Fig. 6a and 6b are characterized by h(M)=27±2 nm, $a_{\Delta f_0}$ (M)=5.2±0.3 Hz/V² and h(N)=50±2 nm, $a_{\Delta f_0}$ (N)=7.8±0.7 Hz/V², respectively. After successive interpolations between different $a_{\Delta f_0}\left(h, \varepsilon_r\right)$ curves, values of ε_r=2.3±0.3 for PS and ε_r=7.5 ±1 were found for PVAc, values in agreement with the macroscopic ones [41]-[43].

Figure 7a shows a quantitative map of the dielectric permittivity of the PVAc/PS film at the nanoscale. The small asymmetry observed on the islands of PVAc on the x axis is most likely attributed to the scanning process (only retrace signal was recorded). An upper limit for the spatial resolution of around 30 nm has been estimated, which corresponds to half the distance necessary to achieve the transition between the dielectric level of the island of PVAc and the matrix of PS (Figure 7b). This value is in good agreement with the theoretical one calculated on the basis of the tip-sample electrostatic interaction [33],[44]: $\Delta x=(R\ z)^{1/2} \sim 20$ nm. This result shows that PS and PVAc are immiscible at scale equal or lower than 30 nm. From the morphology image, we found a surface fraction of PVAc close to 14%, a value coherent with the polymer composition of the film. The direct confrontation of the topography with the dielectric map (Figures 6a and 7a) points out that small satellite nodules around 20 nm are detected in the dielectric map and not in the topography, thus showing the high sensitivity of this method.

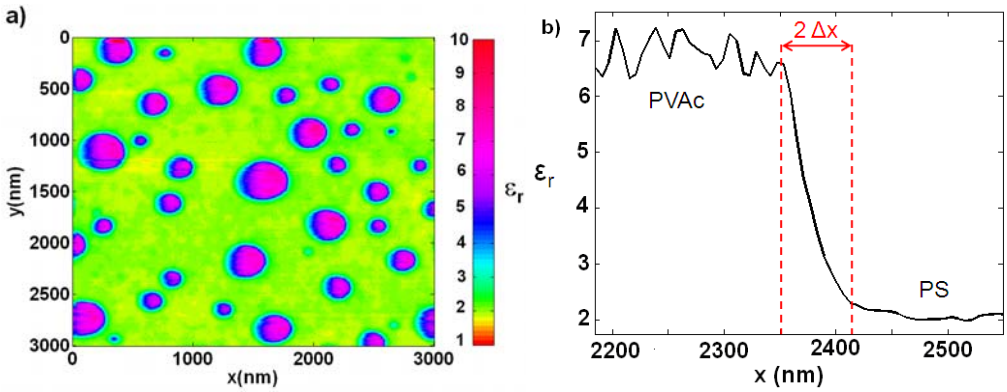

Fig 7: (a) Map of the dielectric permittivity of the PVAc/PS film obtained by processing images shown in Figures 6a and 6b. (b) Typical profile of the dielectric permittivity across the PVAc/PS interface. *Reproduced with permission from C. Riedel et al.[8] © Copyright 2010 American Physical Society.*

3.3 AC experiments

3.3.1 FM-EFM experiments

We turn now to EFM experiments where by applying AC excitation the temperature-frequency dependence of the dielectric response can me measure and analyzed. Experiments were carried out by FM-EFM under Ultra High Vacuum (UHV) with a variable temperature stage (RHK UHV 350). The temperature was measured with a small thermocouple clamped to the sample surface. A classical EFM conducting cantilever with 25 nm tip radius was used. In FM-EFM, the cantilever is oscillated at its resonance frequency, f_0 = 70 kHz, and the resonance frequency shift Δf_0, due to tip-sample interaction forces, is detected with very high resolution using a Nanosurf Easy Phase Locked Loop (PLL) detector. This parameter is used as a feedback for controlling the tip-sample distance z. Additional signals are those measured as a

result of the electrodynamics interaction between the conducting tip and the polymer sample. As the force $\partial F/\partial z$ is proportional to the square of the voltage, a sinusoidal voltage $V_{AC} = V_0 \sin(\omega_e t)$ produces a $2\omega_e$ component response. This component can be detected via the frequency shift of the cantilever by using a lock-in amplifier (Stanford Research SR-830). The obtained signal $V_{2\omega_e}$ is related to $\partial F/\partial z$ (proportional to $G_{2\omega_e}$) by: $V_{2\omega_e} = \frac{A}{4k_c}\frac{\partial F}{\partial z} f_0$ where A is the instrument gain [9]. The force gradient being a function of the dielectric permittivity, any measurable dielectric losses in the material will be detected as a phase shift in the $V_{2\omega}$ signal.

Two different experiments were performed to study successively the thin polymer blend presented in section 3.2.2 (1% w/w in toluene with 75% PS w/w and 25% w/w PVAc). The first is described in references [9] and [10] and consists in recording the phase in one point at different frequencies and constant temperatures. During the acquisition of the dielectric spectrum, the feedback of the PLL detector (typically Δf_0 = 15 Hz) was turned off in order to avoid any coupling with the corresponding electrical frequency. A $V_{AC} = V_0 \sin(\omega_e t)$ voltage at different frequencies varying from 0.1 to 120 Hz was applied between the tip and the sample. It is worth to mention the fact that the frequency range is limited at low frequencies by the time of acquisition and at high frequencies by the bandwidth of the microscope's electronics. A preliminary step consists in measuring the reference phase of $V_{2\omega e}$, Φ_{ref}, at 19°C where both polymers are in the glassy state and have no measurable dielectric relaxation. The difference between this reference situation and the phase measured in the experiments, $\Delta\Phi = \Phi_{ref} - \Phi$, is used to characterize the dielectric dissipation. During the relaxation, due to the loss of energy to align the dipoles in the field, a peak is observed in $\Delta\Phi(\omega_e)$. Using BDS experiments on bulk PVAc, the macroscopic phase of the dielectric permittivity, $\tan^{-1}(\varepsilon''/\varepsilon')$, peaks at about 16° for frequencies between 0.1 and 100 Hz, very close to what was found for $\Delta\Phi(\omega_e)$ of thick films (1 µm) of PVAc using the present FM-EFM technique [9]. For thinner films of PVAc, it was found that the peak in $\Delta\Phi(\omega_e)$ is considerably reduced, to ~ 3° for 50 nm films. This can be understood by recognizing that the force gradient is a complex function of the dielectric permittivity, film thickness, tip radius and tip height that requires numerical modeling [8]. Whereas the macroscopic phase is proportional to fractional increase in permittivity, $\Delta\varepsilon/\varepsilon$, the $\Delta\Phi(\omega_e)$ measured here is proportional to the fractional increase in force gradient, $\Delta(\partial F/\partial z)/(\partial F/\partial z)$. This fraction is found in simulations to be reduced with reduced film thickness due to a larger constant background $\partial F/\partial z$.

Fig. 8 shows $\Delta\Phi(\omega_e)$ over an island of PVAc at different temperatures. The fitting lines were obtained using a Kohlrausch–Williams–Watts response function, $\exp(-t/\tau)^{\beta}$, [45],[46] as a convenient way to describe the experimental result. Maximum value of $\Delta\Phi$ and shape parameter (β=0.42) were fixed by fitting the data measured at 40°C. Keeping these parameters constant and using only a free timescale parameter, a rather satisfactory description of the data was obtained: ie, the shape of the peak does not depend on temperature within the involved uncertainties. The peak frequencies and shape of these peaks are nearly identical to those found in pure PVAc films of similar thickness. Measurements at the same temperatures have been performed over the matrix of PS and the response (not presented in the figure) is always flat ($\Delta\Phi$ < 0.1°). Therefore, the frequency sweep permits to characterize locally the properties of the sample, in good agreement with reference [9]: the matrix is composed of PS whereas islands are domains of PVAc.

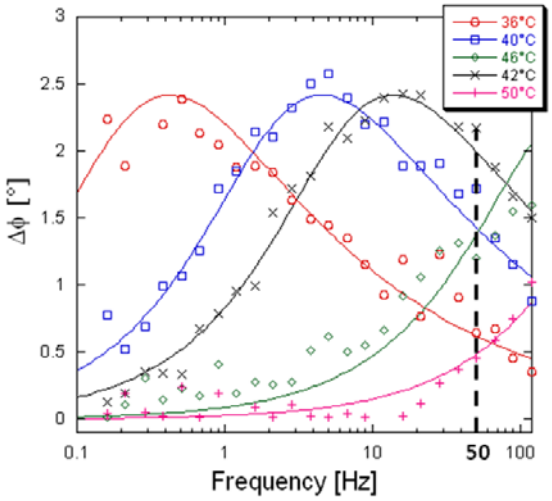

Fig. 8: Phase shift of $G_{2\omega e}$ signals measured in FM-EFM as a function of the frequency over an island of PVAc. Lines are simple description of the data using a KWW like description (see text). Amplitude and shape parameters of all fitting lines were kept constant. The dashed line corresponds to the imaging frequency of Fig. 9a. *Reproduced with permission from C. Riedel et al.[11] © Copyright 2009 American Institute of Physics.*

The second experiment consists in scanning the sample surface while a 50 Hz AC voltage is applied to the tip. In order to keep a constant tip-sample distance, the feedback of the PLL is maintained on. Figures 9(a-f) present images of $\Delta\Phi$ recorded at different temperatures. All images have been rescaled to the same phase shift scale using the WSxM software [47]. The phase recorded on the flat matrix areas is always close to zero, as expected for PS. At 25°C, the image is homogeneous: there is no detectable dielectric relaxation occurring in the islands of PVAc. This demonstrates that this method is not sensitive to topographic effects. When the temperature is increased to 36°C a stronger contrast is observed in the images as the high frequency wing of the dielectric loss peak starts contributing at 50 Hz in the PVAc regions. The maximum contrast is found at 42°C. Further increasing the temperature reduces the contrast as the loss peak shifts to higher frequencies and only the low frequency

contributions are detected. As the shape of the relaxation does not depend significantly on temperature, the contrast observed is attributed to the passage of dynamics associated with the alpha-relaxation through our measurement window. Figure 9g shows the profile of the phase recorded at 42°C. The difference of phase is measured to 2.6°. This value is very similar to that seen in pure PVAc films of similar thickness. All values measured on the maps using a profile are, within experimental errors, the same as those measured using the frequency sweep in one single point at 50 Hz (Fig. 8). The estimated upper limit of the spatial resolution (corresponding to half of the distance necessary to achieve the transition between the dielectric level of PVAc and PS) Δx is around ~40 nm. This value is close to the theoretical resolution given in reference [33], [44] and corresponds to the state-of-the-art resolution in EFM when using standard probes.

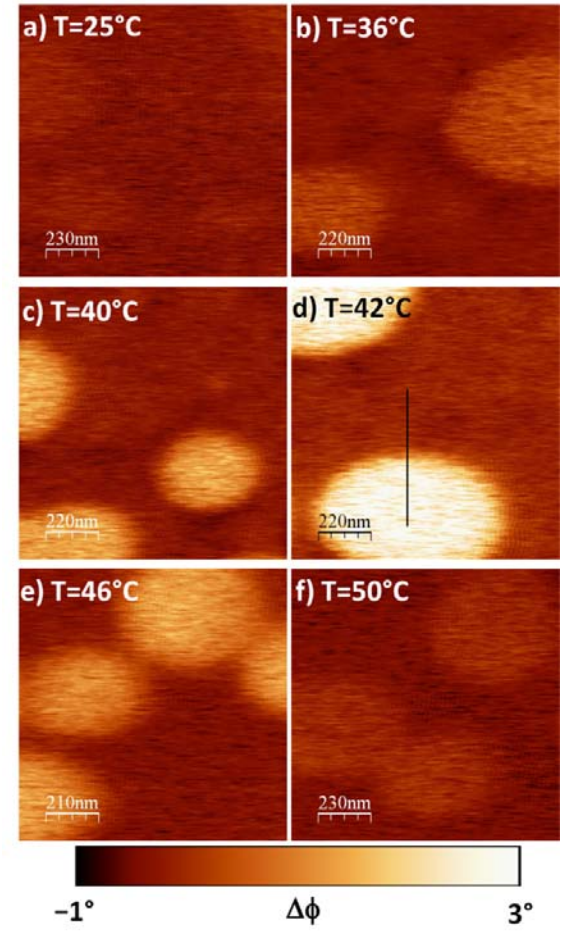

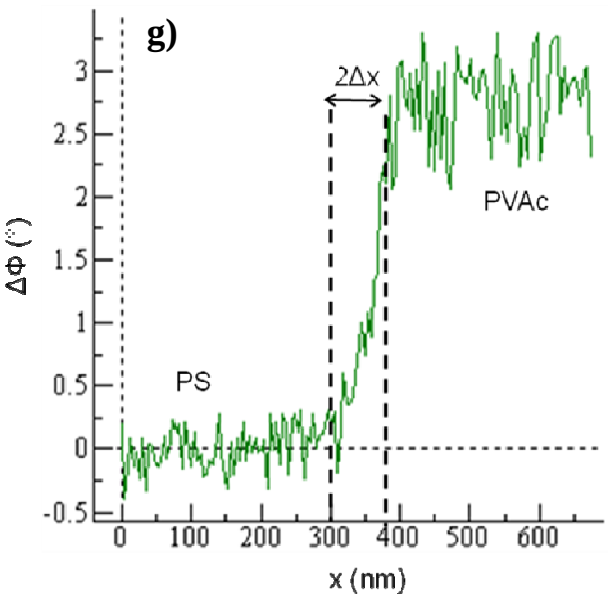

Fig. 9: a-f) FM-EFM images of $\Delta\Phi(\omega_e)$ ($G_{2\omega e}$ phase shifts) recorded at 50 Hz on the thin PS / PVAc film at different temperature. Brighter areas correspond to losses related with the segmental relaxation of PVAc. g) Profile of the phase shift recorded at 50 Hz and 42°. The difference of phase between the matrix of PS and the island of PVAc is of about 2.6°. The lateral resolution Δx is measured around ~ 40 nm. *Reproduced with permission from C. Riedel et al.[11] © Copyright 2009 American Institute of Physics.*

3.3.2 AM-EFM experiments

Finally we present in this section results obtained using AM-EFM. These observations are of great relevance because they demonstrate that FM-EFM and vacuum are not necessary to measure the dynamic dielectric response. This is particularly important to study bio-materials. Such studies can be implemented using standard commercial devices under ambient conditions. Experiments consist in analysing $F_{2\omega_e}$ component by a lock-in amplifier following the procedure described in Fig. 2. Although amplitude and phase of $F_{2\omega_e}$ can be simultaneously recorded, only phase signals are involved in the here presented experimental protocol. As for FM-EFM operations, it is first necessary to measure a reference phase curve $\Phi_{ref}(\omega_e)$, at temperatures where dielectric relaxation of polymers films is negligible. Then, the phase signal $\Phi(\omega_e)$ is acquired at higher temperatures, the difference $\Delta\Phi(\omega_e) = \Phi_{ref}(\omega_e) - \Phi(\omega_e)$ being representative of the loss tangent of the sample. As a demonstration, 250 nm thick pure PVAc films have been investigated (alpha-relaxation). $\Delta\Phi(\omega_e)$ curves measured from 42°C to 55°C at a lift height of 5 nm (z ~ 25 nm) are shown in Fig. 10a. Compared with FM-EFM experiments, similar peak shape (fitted by a KWW function) and height (~ 3°) were observed, but in addition the frequency range has been increased by about 2 decades. Indeed, frequency sweep has been increased up to 30 kHz corresponding to half the resonance frequency of the cantilever. Furthermore, the dynamics (beta-relaxation) of thin films of poly(methyl methacrylate) (PMMA) (Fig. 10b) between 28°C and 69°C has been also studied. 250 nm films were spin-coated starting from 4 % solution of PMMA in toluene. The maximum of the peak in $\Delta\Phi(\omega_e)$ curves is observed to be higher and narrower when increasing the temperature, as observed when

investigating the same material with standard BDS experiments. Concerning the comparison of relaxation time between macro and nano experiments, Crider *et al* [9], [10] have pointed out the fact that the nanoscale relaxation time (i.e. the inverse of the maximum frequency of $\Delta\Phi(\omega_e)$ curve) is shifted to lower values with increasing temperature relative to the bulk values. These results can be interpreted as a small decrease in the dynamical T_g by a few °C or as a speeding up of the alpha relaxation time at T_g. A comparison of the dielectric spectra measured on the same thin sample by EFM and classical BDS as reported in ref [1] and [2] is needed in order to differentiate changes coming from the experimental

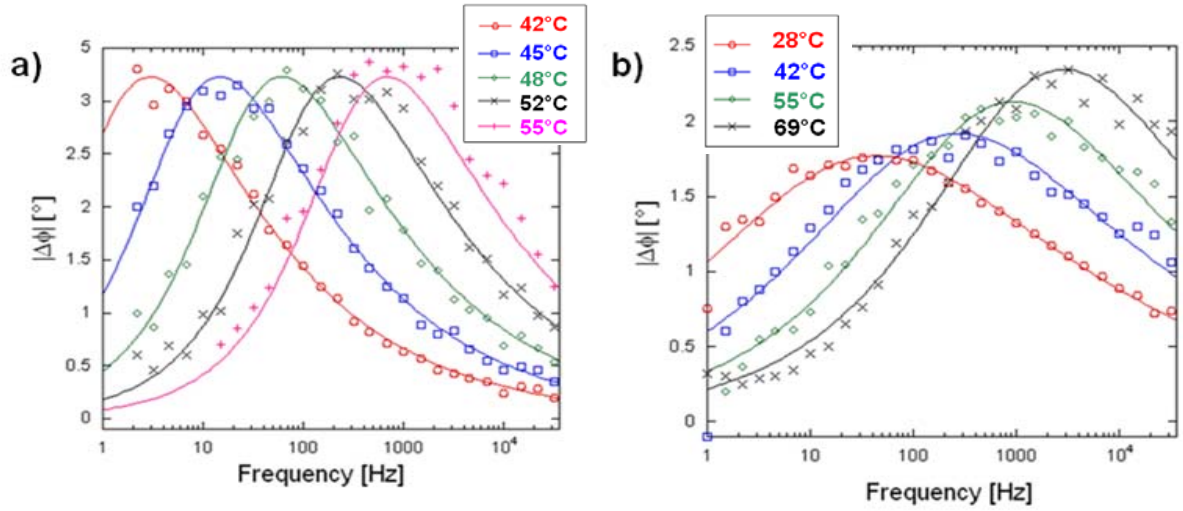

Fig. 10: a) $\Delta\Phi(\omega_e)$ curves ($F_{2\omega e}$ signals phase shifts) measured in AM-EFM as a function of the electrical frequency on a 250 nm pure PVAc film between 42°C and 55°C. b) $\Delta\Phi(\omega_e)$ curves obtained on a 250 nm pure PMMA film between 28°C and 69°C. For both measurements, a lift height of 5 nm has been set during the second pass scan.

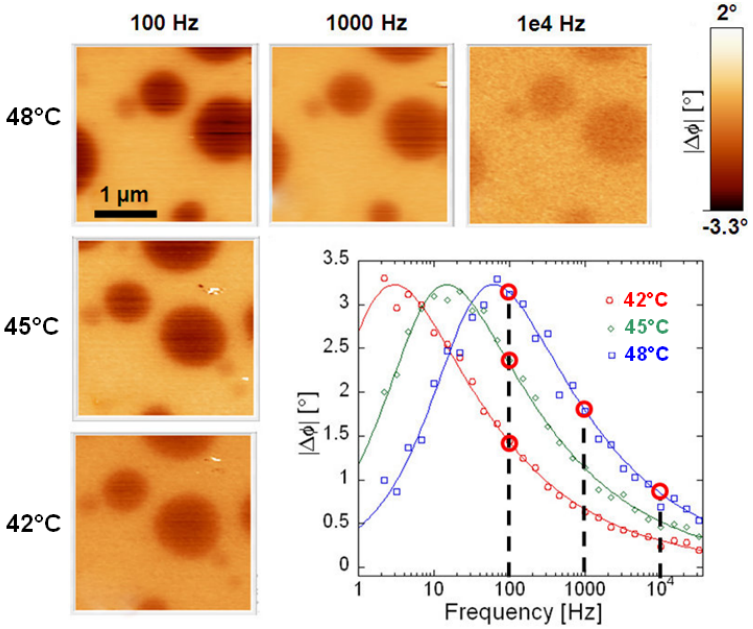

Fig. 11: AM-EFM images of $\Delta\Phi(\omega_e)$ ($F_{2\omega e}$ phase shifts) recorded on a thin PS / PVAc blend sample. In line, images at a fixed temperature and at different frequencies. In column, images at a fixed frequency and different temperatures. Values of frequencies and temperature are chosen according to single point measurements on PVAc shown in the inset. A maximum of contrast is obtained when crossing the alpha-transition of PVAc.

EFM based method from the physical ones coming from the dynamics.

A series of experiments have been carried out on the same PVAc/PS blend samples (4% w/w in toluene with 75% PS w/w and 25% w/w PVAc) used in section 3.2.1 and aiming to image their local dynamics. Two kind of experiments were carried out: the first one at a fixed frequency of 100 Hz and at different temperatures (42°C, 45°C and 48°C) are presented in column in Fig. 11. Frequencies and temperatures were chosen in accordance with single point spectra measured over a PVAc island (inset of Fig. 11). When scanning at 100 Hz over a 3µm×3µm area of the blend sample, a maximum of contrast of PVAc island is clearly observed in $\Delta\Phi$ images at 48°C, in good agreement with single point spectra. Drifts of positioning due to thermal effects are noted on the images but does not affect the proposed interpretation. The second kind of images were recorded at a fixed temperature (48°C) and variable frequency (100 Hz, 1 kHz and 10 kHz). They are presented in line in Fig. 11. As expected the constrast is maximum at 100 Hz and it

deacreases with increasing frequency. In both cases the contrast evolution is always associated with the alpha-relaxation of the PVAc whereas the PS matrix still remains in the glassy state. The obtained spatial resolution is about Δx = 150 nm, which is worse compared with force gradients images (Fig 7 and 9). This can be partly explained by the fact that the resolution in force images is theoretically 30% lower. According to Girard *et al.* in reference [33], $\Delta x = (2Rz)^{1/2}$. Nevertheless, we think that resolution in force images could be improved up to 40 nm by choosing lowest possible lift heights and optimal tips. Thus, the main advantage in using AM-EFM with force detection is its easyness to be implemented in standard devices and the possibility of measuring under different environments.

4. Conclusions

In this chapter, we have described several EFM methods allowing the determination of dielectric properties at the nanoscale. These methods can be classified in different categories, following the excitation type (AC or DC) and following the detection method (force or force gradient), as summarized in table 1. DC methods are well adapted to determine quantitatively the dielectric permittivity ε_r of insulating layers. We have presented a simple numerical approach, called equivalent charge model (ECM). Some examples of polymer thin films studied at different temperatures have been also presented. In particular, concerning PVAc films, we have shown evidence of a big difference of ε_r below and above T_g . AC methods can provide qualitative informations on the temperature-frequency dependence of dielectric properties. After having developed nanodielectric spectroscopy in one single point, we have seen how to extend it to image the dynamics of nanostuctured polymers. As an example, the alpha-relaxation of PVAc islands in a matrix of PS has been imaged. These experiments have been first achieved by FM-EFM under vacuum and later on carried out using AM-EFM at room conditions. These last results are of first importance because they open the way to experiments easier to implement with standard AFM. In the near future, studies of the local dielectric response of biological materials or other soft matter materials should be thus possible. From the spatial resolution point of view, force gradient detection methods have provided the best defined images (20 to 40 nm). We also think that a comparison can be done on the adaptability level of the method to investigate one specific aspect. Nevertheless, we have shown in this chapter that these methods could be adapted to multiple problems.

		Excitation Type	
		DC	**AC**
Detection method	**Force**	**F_{DC}** [6] ♦ Control of the probe-sample distance : Static force mode, Constant height, Single pass ♦ Quantitative imaging of ε_r on SiO_2/Au films and purple membrane monolayers	**$F_{2\omega e}$** [C. Riedel *et al* to be published] ♦ Control of the probe-sample distance : AM-EFM, Double pass ♦ Nanodielectric spectroscopy of PVAc and PMMA thin films ♦ Imaging of the temperature-frequency dependence of the dynamics of nano-structured PVAc/PS films
	Force gradient	**G_{DC}** [7],[8] ♦ Control of the probe-sample distance : AM-EFM, Double pass ♦ Single point measurement of ε_r on polymers films (PVAc, PS) at different temperatures ♦ Quantitative imaging of ε_r on nano-structured PVAc/PS films	**$G_{2\omega e}$** [9]-[11] ♦ Control of the probe-sample distance : FM-EFM, Single pass ♦ Nanodielectric spectroscopy of PVAc thin films ♦ Imaging of the temperature-frequency dependence of the dynamics of nano-structured PVAc/PS films

Table 1: Different EFM methods to determine the dielectric properties at nanoscale, classified following the excitation type and the detection method. Numbers in brackets indicate the corresponding references.

Acknowledgements:

The financial support of Donostia International Physics Center DIPC is acknowledged. The authors would also like to acknowledge the financial support provided by the Basque Country Government Reference No. IT-43607, Depto. Educación, Universidades e Investigación, the Spanish Ministry of Science and Innovation Grant No. MAT 2007-63681, the European Community SOFTCOMP program, the PPF Rhéologie et plasticité des matériaux mous hétérogènes 2007–2010, Contract No. 20071656 and the National Science Foundation (Grant No. NSF DMR-0606090).

References:

[1] A. Serghei, M. Tress, F. Kremer, Macromolecules **39**(26), 9385 (2006).
[2] S. Napolitano, V. Lupascu, M. Wübbenhorst, Macromolecules **41**(4), 1061 (2008).
[3] A. V. Krayev and R.V. Talroze, Polymer **45**, 8195-8200 (2004).

[4] A. V. Krayev, G. A. Shandryuk, L. N. Grigorov and R. V. Talroze, Macromol. Chem Phys. **207**, 966 (2006).
[5] L. Fumagalli, G. Ferrari, M. sampietro and G. Gomila. Nano Letters **9**(4), 1604-1608. (2009).
[6] G. Gramse, I. Casuso, J. Toset, L. Fumagalli, and G. Gomila, Nanotechnology **20**, 395702 (2009).
[7] C. Riedel, R. Arinero, P. Tordjeman, M. Ramonda, G.Lévêque, G. A. Schwartz, D. Garcia de Oteyza, A. Alegria, and J. Colmenero, J. Appl. Phys. 106, 024315 2009.
[8] C . Riedel, R. Arinero, P. Tordjeman, G. Lévêque, G.A. Schwartz, A. Alegría and J. Colmenero. Physical Review E (R) **81**(1): 010801. (2010) ; C. Riedel, G. A. Schwartz, R. Arinero, P. Tordjeman, G. Lévêque, A. Alegria, J. Colmenero, Ultramicroscopy **110** 634–638 (2010).
[9] P. S. Crider, M. R. Majewski. J. Zhang, H. Oukris, N. E. Israeloff, Applied Physics Letters, **91**, 013102 (2007)
[10] P. S. Crider, M. R. Majewski, J. Zhang, H. Oukris and N. E. Israeloff. J. Chem. Phys. **128**, 044908 (2008).
[11] C. Riedel, R. Sweeney, N. E. Israeloff, R. Arinero, G. A. Schwartz, A. Alegria, P. Tordjeman and J. Colmenero, Applied Physics Letters, **96**, 213110 (2010).
[12] J. Hu, X. D. Xiao, D. F. Ogletree, M. Salmerón, Science, **268**, 267-269 (1995).
[13] H.W. Hao, A. M. Baró, J. J. Sáenz, J. Vac. Sci. Technol. B, **9**(2), 1323-1328 (1991).
[14] B. D. Terris, J. E. Stern, D. Rugar, H. J. Mamin, Phys. Rev. Lett., **63** (24), 2669-2672 (1989).
[15] L. H. Pan, T. E. Sullivan, V. J. Peridier, P. H. Cutler, N. M. Miskovsky, Appl. Phys. Lett., **65**, 2151-2153 (1994).
[16] T. Hochwitz, A. K. Henning, C. Levey, C. Daghlian, J. Slinkman, J. Vac. Sci. Technol. B, **14**, 457-462 (1996).
[17] S. Hudlet, M. Saint Jean, C. Guthmann, J. Berger, Eur. Phys. J. B, **2**, 5-10 (1998) .
[18] J. Colchero, A. Gil, A. M. Baró., Phys. Rev. B, **64**, 245403 (2001).
[19] G. Gomila, J. Toset and L. Fumagalli, Journal of Applied Physics, **104**, 024315 (2008)
[20] G. Mesa, E. Dobado-Fuentes, J. J. Sáenz, J. Appl. Phys., **79**, 39-44 (1996)
[21] S. Belaidi, P. Girard, G. Leveque, J. Appl. Phys., **81** (3), 1023-1030 (1997).
[22] G. M. Sacha, E. Sahagun, and J.J. Saenz, Journal of Applied Physics, **101**(2), p. 024310 (2007).
[23] E. Durand, Electrostatique, tome III, Masson, Paris, p.233 (1966).
[24] S. Gómez-Moñivas, J. J. Sáenz, Appl. Phys. Lett., **76**, 2955-2957 (2000).
[25] S. Gómez-Moñivas, L. Froufe-Pérez, A. J. Caamaño, J. J.Sáenz, Appl. Phys. Lett., **79**, 4048-4050 (2001).
[26] G. M. Sacha, C. Gómez-Navarro, J. J. Sáenz, J. Gómez-Herrero, Appl. Phys. Lett., **89**, 173122 (2006).
[27] S. Belaidi, E. Lebon, P. Girard, G. Leveque, S. Pagano, Appl. Phys. A, **66**, S239-S243 (1998).
[28] Z. Y. Li, B. Y. Gu, G. Z. Yang, Phys. Rev. B, **57**, 9225-9233 (1998).
[29] E. Strassburg, A. Boag, Y. Rosenwaks, Rev. Sci. Instrum., **76**, 083705 (2005).
[30] Y. Martin, D. W. Abraham, and H. K. Wickramasinghe, Appl. Phys. Lett. **52**, 1103 (1988).
[31] B. D. Terris, J. E. Stern, D. Rugar, and H. J. Mamin, Phys. Rev. Lett. **63**, 2669 (1989).
[32] P. Girard, M. Ramonda, and D. Saluel, J. Vac. Sci. Technol. B **20**, 1348 (2002).
[33] P. Girard and A. N. Titkov in Applied scanning probe methods II, B. Bhushan, H. Fuchs, Springer, p.312 (2003).
[34] L. Manzon, P. Girard, R. Arinero, M. Ramonda, Review of Scientific Instruments, **77**, 096101 (2006)
[35] G. A. Schwartz, E. Tellechea, J. Colmenero and A. Alegría, J. Non-Cryst. Sol. **351**, 2616 (2005).
[36] G. A. Schwartz, J. Colmenero y A. Alegría, Macromolecules **39**, 3931 (2006).
[37] G. A. Schwartz, J. Colmenero y A. Alegría, Macromolecules **40**, 3246 (2007).
[38] G. A. Schwartz, J. Colmenero y A. Alegría, J. Non-Cryst. Sol., **353**, 4298 (2007).
[39] M. Tyagi, J. Colmenero y A. Alegría, J. Chem. Phys., **122**, 244909 (2005).
[40] D. Hall, P. Underhill, and J. M. Torkelson, Polymer Engineering and Science, **38**, 2039 (1998).
[41] N. G. McCrum, B. E. Read, and G. Williams, "Anelastic and dielectric effects in polymeric solids." Dover (1991).
[42] J. M. O´Reilly Journal of Polymer Science, **57**, 429 (1962).
[43] O. Yano, and Y. Wada, Journal of Polymer Science Part A-2 - Polymer Physics **9**, 669 (1971).
[44] S. Gomez-Monivas, L. S. Froufe, R. Carminati, J. J. Greffet and J. J. Saenz Nanotechnology **12**, 496 (2001).
[45] R. Kohlrausch, Poggendorff **91**:56–82, 179 (1854).
[46] G. Williams and D. C. Watts, Transactions of the Faraday Society **66**:80 (1970).
[47] I. Horcas, R. Fernandez, J. M. Gomez-Rodriguez, J. Colchero, J. Gomez-Herrero, A. M. Baro. Review of Scientific Instruments **78** (1): 013705. (2007).